THE JOURNAL OF PHYSICAL CHEMISTRY C

ARTICLE

pubs.acs.org/JPCC

Using Pentaarylfullerenes to Understand Network Formation in Conjugated Polymer-Based Bulk-Heterojunction Solar Cells

Christopher J. Tassone, Alexander L. Ayzner, Robert D. Kennedy, Merissa Halim, Monica So, Yves Rubin,* Sarah H. Tolbert,* and Benjamin J. Schwartz*

Department of Chemistry and Biochemistry, UCLA, Los Angeles, California 90095-1569, United States

ABSTRACT: We have synthesized a series of pentaarylfullerene derivatives and incorporated them into bulk-heterojunction (BHJ) solar cells using poly(3-hexylthiophene) as the electron donating material. Through a combination of grazing incidence X-ray diffraction and atomic force microscopy we see two distinct nanoscale morphologies emerge across the series. Investigating the device physics using $J-V$ characterization, light intensity dependence, and fluorescence quenching studies, we are able to correlate the morphology to the device physics. This has afforded the opportunity to clearly see how altering the nanoscale phase segregation can change the distinct physical processes occurring within a BHJ solar cell. We observe an order of magnitude increase in the efficiency of devices that utilize self-assembling fullerene derivatives over their nonassembled counterparts. More importantly, however, these results allow us to shed light on the mechanism behind this differential phase segregation using a fullerene self-assembly model. On the basis of the data, we propose new design rules for the structure of future generations of fullerene electron accepting materials for use in BHJ solar cells.

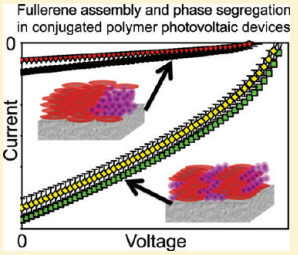

INTRODUCTION

Organic photovoltaics have been studied extensively over the past decade, largely because of the ease with which they can be manufactured and the fact that it is possible to deposit them on flexible substrates, which offers exciting possibilities for commercial production.[1−3] To date, devices based on conjugated polymers as electron donors and fullerene derivatives as electron acceptors have yielded the highest power conversion efficiencies.[4,5] In a typical device, light absorption by the polymer leads to the creation of strongly bound, mobile excited states called excitons. The distance over which excitons can migrate during their lifetime has been the subject of some debate, but the current literature consensus is in the range of 5−20 nm.[6,7] If an exciton can reach one of the fullerene acceptor molecules during its lifetime, the energy difference between the LUMO of the polymer and the LUMO of the fullerene derivative helps promote rapid electron transfer, yielding a hole localized on the polymer and an electron on the fullerene derivative. Finally, a photocurrent is produced in the external circuit as long as the photogenerated carriers have a continuous pathway on each of their respective phases to reach the device electrodes.

One of the challenges of producing polymer-based photovoltaics is to control the nanometer-scale morphology of the two active components. The dual requirements of interspersing acceptor molecules on a fine enough length scale to harvest all excitons, while also maintaining the conductive pathways needed to collect the separated charges, must be satisfied simultaneously. The typical method for producing such devices is to make the active layer a bulk heterojunction (BHJ) by simply blending the two components together and allowing spontaneous phase segregation to produce the ideal morphology.[8] In addition, more controlled, alternate processing procedures also have been studied.[9,10] The nanometer-scale morphology of BHJ blends can be varied by changing parameters such as the time and temperature of thermal annealing[11,12] or by using solvent additives during spin-coating.[13,14] To make meaningful advances in device performance, however, one must repeatedly optimize processing conditions to produce the best morphology for any set of new materials. This is a painstaking process that currently is still carried out through trial and error.

By far the most studied combination of components in BHJs has been regioregular poly(3-hexylthiophene-2,5-diyl) (P3HT) as the polymer electron donor and phenyl-C_{61}-butyric acid methyl ester ([60]PCBM) as the electron acceptor fullerene derivative. The most efficient devices produced recently have made use of redder-absorbing polymers with either [60]PCBM or its C_{70} analogue, [70]PCBM.[15] The use of red-absorbing polymers has made it clear that changing the polymer electronic structure can lead to significant improvements in device performance.[15] The way device performance changes when using different fullerene derivatives, however, can be unpredictable: although it is known that the way the fullerene is functionalized can alter its LUMO level and thus the device open circuit voltage (V_{oc}),[16−18] the manner via which spontaneous phase separation takes place depends on the subtle balance of many variables, including the nature of the fullerene side groups.[16] This is because the formation of an interpenetrating network that is conducive to efficient carrier transport requires that some spontaneous phase separation occur: the polymer and the fullerene cannot be completely miscible. Excessive phase separation, on the other

Received: August 2, 2011
Revised: October 4, 2011
Published: October 05, 2011

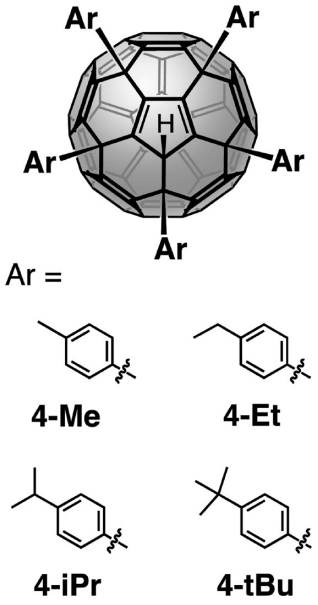

Figure 1. Generalized structure of PAF derivatives, with the specific aryl substitutions for the molecules used in this study shown below.

hand, destroys the nanoscale network and reduces device efficiency.[19,20] Thus, even though [60]PCBM and [70]PCBM were first used in polymer-based solar cells over a decade ago,[8,21] these two compounds have remained the gold standards for the electron acceptors in BHJ devices because it is unclear how differing degrees of phase separation affect BHJ morphology when using alternate fullerene derivatives.

The goal of this study was to use a well-defined series of related fullerene derivatives to show one systematic route to optimizing device performance with fullerene derivatives that are chemically very different from PCBM. Specifically, we have focused on the use of self-assembling fullerene derivatives to understand how control over nanoscale morphology influences device performance. We note that these fullerenes are not optimized for all aspects of device performance, so the devices produced here show only moderate efficiencies. The trends in the data, however, add significant clarity to the complex changes that occur in the structure of a BHJ solar cell when novel fullerenes are substituted for PCBM.

To facilitate this exploration, we elected to build upon previous work in which we explored the properties of solar cells based on P3HT in BHJ blends with self-complementary pentaarylhydrofullerenes (PAFs), which have a molecular shape resembling badminton shuttlecocks.[22] PAFs with different substituents show very different intermolecular morphologies in single-crystal X-ray diffraction studies, as we recently have shown.[23] Most importantly for this work, fullerenes with well-defined cavities are consistently able to assemble into "stacks" in crystals.[24] Because of this, they provide a novel route to probe the relationship between the nanometer-scale morphology of BHJ blends and the chemical structure of a fullerene-derived acceptor. In what follows, we present the results of an extensive optoelectronic and structural characterization of a series of BHJ solar cells utilizing regioregular P3HT as the donor and a series of PAF acceptors. Each PAF has essentially identical frontier molecular orbitals and a systematically varied substituent structure, as shown in Figure 1. We find that relatively small changes in the chemical structure of the PAFs result in dramatic differences both in the degree of polymer/fullerene phase segregation and in device efficiencies. On the basis of the results, we argue that it is not the solubility of the fullerene in organic solvents that determines device performance, as has been argued previously.[15] Rather, the relative device efficiency can be rationalized by a combination of the solubility of the fullerene in the *polymer phase* and the kinetics of polymer/fullerene phase separation. It is these kinetics, in particular, that can be modified using self-assembly, with self-complementary structures showing significantly less large-scale fullerene crystallization.

EXPERIMENTAL SECTION

All BHJ photovoltaic devices in this work were prepared by first cleaning prepatterned tin-doped indium oxide (ITO; TFD Inc.) substrates with successive sonication in laboratory-grade detergent (Alconox) solution, 18 MΩ water, acetone, and finally isopropyl alcohol for ∼10 min each. The substrates were then treated with an air plasma (200 mTorr) for 10 min prior to spin-coating a ≤50 nm layer of poly(ethylenedioxythiophene):poly-(styrenesulfonic acid) (PEDOT:PSS, HC Starck Inc. PH 500) at 5000 rpm for 60 s under ambient conditions. The PEDOT:PSS-coated slides were then baked on a digitally controlled hot plate in a nitrogen atmosphere for 20 min at 140 °C.

The active layers in the photovoltaic devices were cast from blend solutions of regioregular P3HT (Rieke Metals EE 4000 series, nominally 90−93% regioregular) and various PAFs in *o*-dichlorobenzene (ODCB) at a P3HT concentration of 1% w/w. We refer to the different PAFs, whose synthesis and crystal structures are described elsewhere,[23] by the nature of the alkyl group in the 4-position of the pentaaryl substituents; our naming convention is summarized in Figure 1. The polymer:PAF weight ratio used for the P3HT:**4-tBu** solution was 1:0.45, while those for the other PAFs were 1:0.43 P3HT:**4-iPr**, 1:0.40 P3HT:**4-Et**, and 1:0.35 P3HT:**4-Me**, chosen to ensure that the solutions for all four PAFs were mole matched. All of the P3HT:PAF solutions were heated to 55 °C for several hours in a nitrogen atmosphere to aid dissolution. After being cooled to room temperature, the P3HT:PAF solutions were passed through a 0.45 μm PTFE filter before being spin-cast at 1000 rpm for 90 s onto the PEDOT:PSS-coated substrates described above.

Prior to deposition of the cathode, the P3HT:PAF BHJ films were annealed on a digitally controlled hot plate at 150 °C for 20 min in an argon atmosphere; samples were covered with a shallow Petri dish during annealing to help ensure uniform heating. At the end of the 20 min annealing cycle, the devices were rapidly cooled to room temperature by placing them onto a metal surface. The cathode was then deposited at a pressure of $\sim 10^{-6}$ Torr by evaporating 40 nm of calcium metal followed by a 10 nm aluminum protective layer onto the completed BHJs through a shadow mask, resulting in active device areas of 6.5 mm^2.

We measured the photovoltaic performance of the resultant devices in an argon atmosphere using a Keithley 2400 source meter and a xenon arc lamp equipped with a liquid light guide and an AM-1.5 filter (Oriel) as the excitation source. The illumination intensity was adjusted using a set of neutral density filters to be 100 mW/cm^2 (1 sun). For each PAF, we tested approximately 50 devices to ensure reproducibility.

Photoluminescence (PL) intensity from the active layers in our devices was measured by exciting the films with 530 nm light through the transparent ITO electrode; integration times were

kept short enough to avoid any measurable degradation of the polymer PL during the course of the experiment. For these experiments, the sample normal was positioned at 70° with respect to the excitation beam, and the PL was detected in a front-face geometry at ~22° with respect to the excitation beam. All PL spectra were normalized by the optical density of the film at 530 nm and corrected for the monochromator and detector responsivity.

Structural characterization of our P3HT:PAF BHJ films was carried out using both two-dimensional grazing-incidence X-ray diffraction (2D-GIXD) and atomic force microscopy (AFM). GIXD experiments were performed at the Stanford Synchrotron Radiation Lightsource on beamline 11-3 using an X-ray wavelength of 0.9742 Å. Data were collected on films prepared in an identical manner to those described above except that single crystal silicon substrates were used rather than ITO in order to prevent diffraction from the substrate. The 2D data were integrated over the azimuthal angle to yield intensities as a function of scattering vector, q, and presented in a 1D fashion here in order to more clearly visualize the nature of the polymer and PAF crystallinity in each film. AFM experiments were performed using a Nanoscope V multimode scanning probe microscope (Veeco Digital Instruments) operating under ambient conditions. Antimony n-doped silicon cantilevers (TESP, Veeco Probes) with spring constants of 42 N/m, first longitudinal resonance frequencies between 230 and 410 kHz, and nominal tip radii of 8 nm were employed in tapping mode. Simultaneous height and phase images were acquired, and all data were reproduced across multiple samples.

RESULTS

As discussed above, we chose to work with a series of pentaarylfullerenes (PAFs) in order to systematically probe the influence of fullerene chemical structure on the morphology of semiconducting-polymer thin film BHJs. Our choice was based both on the facile synthesis of these derivatives, which affords very pure compounds with high yields, and on the fact that some of these molecules show self-assembly behavior in the solid state.[22,24] This combination of properties allows us to produce a family of related molecules with different propensities to self-organize. Figure 1 shows the chemical structures of the four derivatives that are the focus of this work; the pentarylhydrofullerenes have a 6, 9, 12, 15, 18 addition pattern which isolates a cyclopentadiene unit from the remaining contiguous 50-π electron framework. The four molecules differ only in the alkyl group at the para position of the phenylene rings: methyl (**4-Me**), ethyl (**4-Et**), isopropyl (**4-iPr**), and *tert*-butyl (**4-tBu**) groups. The frontier molecular orbitals of these molecules are virtually identical; calculations suggest that the LUMO is localized on the spherical carbon cage with negligible orbital coefficient located on the aryl addends.[20] We have confirmed this conclusion on these PAFs using cyclic voltammetry (CV), which shows an identical LUMO energy for all four derivatives.[24] We also expect that the permanent dipole moment and polarizability should not change with the different alkyl substitutions due to their relative electronic isolation from the π-conjugated spherical core. Thus, the main difference between the four derivatives is in their effective van der Waals interaction surface, which changes because of the different sizes and shapes of the alkyl groups.

Photovoltaic Performance. To understand how the relatively subtle differences in molecular shape and packing of the PAFs affect the performance of photovoltaic devices, we prepared solar cells containing P3HT blended with each of the PAF derivatives at the same molar polymer:PAF ratio using the methods described above. Figure 2 shows the current density (J)/voltage (V) characteristics of our P3HT:PAF solar cells; the performance characteristics of these devices are also summarized in Table 1. The open-circuit voltage (V_{oc}) is ~1 V for all four PAFs; this relatively high value for V_{oc} is consistent with the fact that the LUMO of the pentaarylhydrofullerenes is higher in energy than that of methanofullerenes such as [60]PCBM. Multiple substitutions to the fullerene cage are known to raise both the energy of the fullerene LUMO and the V_{oc} of resulting devices.[25]

More interesting than the trends in V_{oc}, however, are the trends in current density, as this value differs greatly for devices fabricated using different PAFs. In fact, the $J-V$ curves fall into two distinct groups: **4-Me** and **4-Et** give quite low short-circuit currents (J_{sc}), whereas **4-iPr** and **4-tBu** yield J_{sc} values that are approximately 6 times higher. We do not believe that the differences in the photocurrent magnitudes that we observe are due to differences in the intrinsic electron mobilities of the PAFs. For pure fullerenes with similar packing densities, we would

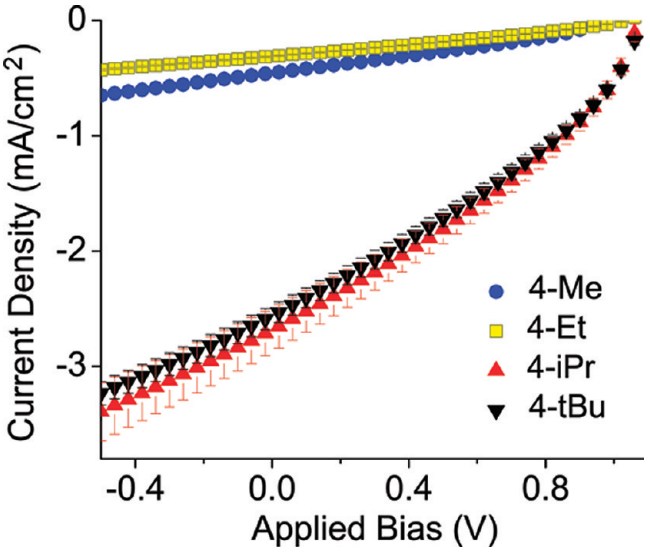

Figure 2. Current density−voltage characteristics under AM 1.5 illumination of thermally annealed BHJ solar cells comprised of regioregular P3HT blended with various PAF fullerene derivatives. The four curves separate into two sets, with one set displaying low currents (**4-Me** (blue circles) and **4-Et** (yellow squares)), while the other set has current densities that are ~5 times greater (**4-tBu** (black point-down triangles) and **4-iPr** (red point-up triangles)). The differences in PV performance are due to differences in nanometer-scale morphology since the electronic structure of the four PAF derivatives is essentially identical. All devices show a nearly constant V_{oc} of ~1 V.

Table 1. Performance Parameters of ITO/PEDOT:PSS/P3HT:PAF/Ca/Al Solar Cells under AM 1.5 Illumination

PAF	P3HT:PAF weight ratio	J_{sc} (mA/cm^2)	V_{oc} (V)	FF (%)	PCE (%)
4-Me	1/0.35	0.45	0.96	31.7	0.14
4-Et	1/0.41	0.31	1.02	29.7	0.1
4-iPr	1/0.43	2.7	1.08	33.4	0.97
4-tBu	1/0.45	2.6	1.08	32.9	0.92

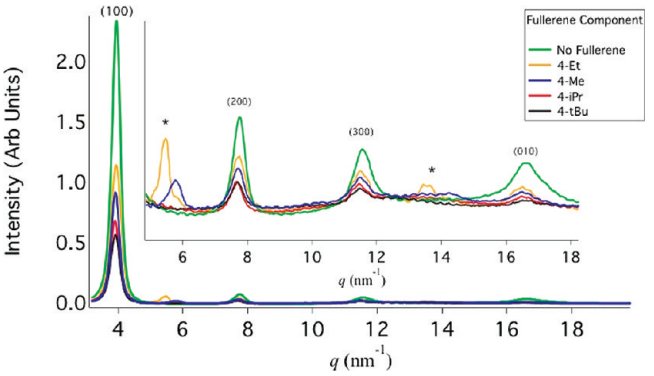

Figure 3. One-dimensional GIXD data for BHJ films composed of P3HT blended with various PAFs as well as a pure polymer film. The inset provides an expanded view of the diffraction from 5 to 18 nm^{-1} in order to more clearly see the high-q diffraction peaks. For all films presented here the (100), (200), (300), and (010) P3HT peaks are labeled on the graph. Diffraction peaks labeled with a star are associated with scattering from the fullerene. In the case of the P3HT:**4-tBu** and P3HT:**4-iPr** BHJs, no fullerene diffraction is observed, indicating that the fullerene in these films is amorphous. However, for the **4-Me** and **4-Et** composite films, two fullerene diffraction peaks are observed between 5 and 6 nm^{-1} and 13 and 15 nm^{-1}. This indicates that crystalline fullerene exists within these composite films.

expect electron transfer rates to be higher among the derivatives with the smallest alkyl substituents, since bulky alkyl groups are more likely to inhibit electron transport. However, this is the opposite of what we observe, with higher short circuit currents obtained in the PAFs with the largest alkyl groups. Thus, as argued below, we believe that the differences in photovoltaic performance come from different network morphologies produced by the differences in the alkyl groups at the peripheries of the PAFs.

Structural Characterization. To better understand the reasons for the dramatic differences in device performance, we have examined the differing extent of phase segregation in the P3HT:PAF films using 2D-GIXD. Figure 3 shows one-dimensional integrations of two-dimensional GIXD data for annealed BHJ films of each PAF blended with P3HT as well as that of a pure P3HT film. Textural information is obtained by performing the integration of 15° slices corresponding to either out-of-plane diffraction (i.e., lattice planes parallel to the substrate) or in-plane diffraction (lattice planes perpendicular to the substrate). Diffraction from the pure P3HT film shows crystalline features in the out-of-plane direction corresponding to the (100), (200), and (300) peaks of crystalline P3HT at 3.9, 7.8, and 11.7 nm^{-1}, respectively. The data thus indicate that the polymer chains are oriented edge-on with respect to the substrate. The (010) peak is observed to lie in the in-plane direction of the film at 16.4 nm^{-1}. This indicates that the polymer chains in the crystallites are predominantly oriented with the long axis of the polymer parallel to the substrate. We note that this preferred orientation of the polymer is seen in all of the P3HT:PAF films and also has been observed previously in P3HT:[60]PCBM bulk-heterojunction films,[26,27] indicating that the presence of fullerene derivatives does not significantly perturb the natural orientation of P3HT crystallites in spin-cast films.

Since the basic orientation of the P3HT crystallites is the same in all of the films, it is possible to quantify the degree of crystallinity of both pure polymer and the PAF containing BHJs simply by comparing the magnitudes of the different diffraction peaks. Inspection of the P3HT (100) peak makes it clear that the addition of any of the PAFs dramatically reduces the crystallinity of the P3HT. This result is expected, as mixing of the polymer and the fullerene in a BHJ inhibits the formation of large crystalline domains of pure polymer. More interesting is the fact that the degree of P3HT crystallinity is quite different when the polymer is blended with different PAFs: the polymer crystallinity is greatest when P3HT is blended with the **4-Et** and **4-Me** PAFs. In contrast, the polymer diffraction peaks for blends of P3HT with **4-iPr** and **4-tBu** PAFs have significantly reduced intensity. To determine whether these changes in polymer crystallinity result from differences in the average crystallite size or in the number of P3HT crystallites, we examined the width of the polymer (100) peak and used the Scherrer equation[28] to estimate the crystallite size. This analysis, which assumes zero crystalline disorder, yielded average polymer crystallite sizes of 24, 20, 23, and 22 nm for **4-Me**, **4-Et**, **4-iPr**, and **4-tBu**, respectively. The fact that there is little change in the average crystallite size strongly suggests that the differences in diffraction peak intensity result from changes in the total amount of crystalline P3HT present in the BHJ films. Thus, the polymer simply has more amorphous and less crystalline regions when blended with **4-iPr** or **4-tBu** than when blended with **4-Me** or **4-Et**.

It has been argued that crystallization of the individual components of a BHJ is what drives phase segregation and, consequently, the nanometer-scale morphology of the blend.[29,30] As a result, the extent of phase separation can be directly correlated with the strength of the P3HT diffraction in a polymer/fullerene BHJ.[11] On the basis of this reasoning, our data indicate a high degree of phase segregation in BHJs fabricated with **4-Et** or **4-Me** and much less phase segregation for devices fabricated with **4-iPr** or **4-tBu**.

Further support of this conclusion can be found by examining diffraction from the PAF itself, rather than from the P3HT, again using 2D-GIXD. The nonindexed peaks (starred) in the inset of Figure 3 correspond to diffraction from the fullerene. For the P3HT:**4-Et** BHJ, the yellow trace in the inset to Figure 3 shows a diffraction peak from **4-Et** crystallites at 5.4 nm^{-1} as well as a broad feature that most likely results from a combination of several PAF diffraction peaks centered near 13.9 nm^{-1}. Similarly, for P3HT blends with **4-Me**, a peak is observed at 5.7 nm^{-1} with a second, broader peak observed at 14.2 nm^{-1}. In the case of both **4-tBu** and **4-iPr**, however, we observed no diffraction from the PAF component. Thus, it appears that crystallization of the PAF helps to drive phase segregation in the **4-Me** and **4-Et** P3HT:PAF BHJ films.

To better visualize the crystallites in the P3HT:PAF blends and to examine phase separation of noncrystalline components, we used phase-contrast tapping-mode atomic force microscopy (AFM), for which select images are shown in Figure 4. The images of all four BHJ films show small, ricelike features with a ~10 nm length that are known from the literature to be nanocrystalline domains of P3HT.[31] In the images of the BHJs formed from **4-Me** and **4-Et**, there are also large, roughly rectangular regions that we believe correspond to crystallites of the PAF. This conclusion is based on two facts. First, these two films show significant X-ray diffraction from the PAF. Second, the films contain only P3HT and PAF; P3HT has never been reported to produce crystals with a form factor observed in our AFM images and the X-ray diffraction indicates that P3HT crystallites do not exceed ~25 nm in size. These crystalline

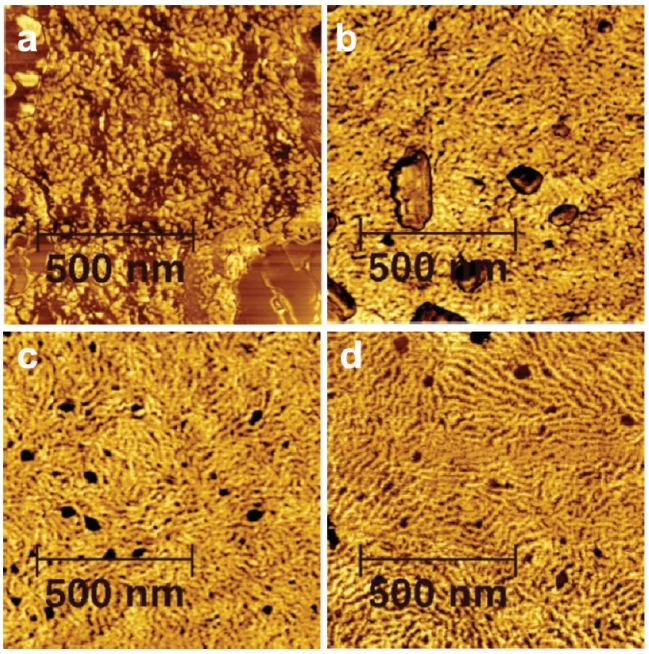

Figure 4. Tapping mode AFM phase images for annealed P3HT:PAF BHJ films. Three distinct types of features can be observed in these images. The bright ricelike grains observed in all four images correspond to nanocrystalline P3HT. In the case of the **4-Et** (a) and the **4-Me** (b) composites, large fullerene crystallites are visible sitting on top of the bulk of the film. These crystalline fullerene features cover almost the entirety of the film surface, though the density is higher for films produced with **4-Et** than with **4-Me**. By contrast, amorphous fullerene regions appear as 10−20 nm diameter dark circular features that are interspersed in the P3HT matrix in the **4-iPr** (c) and **4-tBu** (d) blend films. For the **4-iPr** and **4-tBu** composites, no crystalline fullerene is observed.

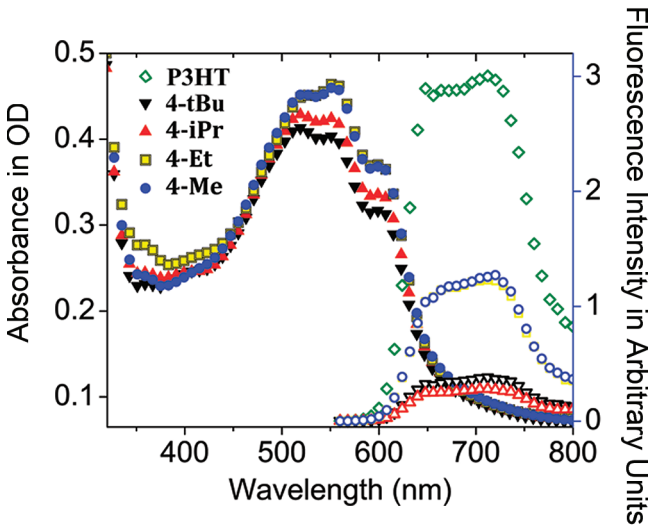

Figure 5. UV−visible absorption (left, filled symbols) and PL (right, open symbols) spectra of P3HT/PAF blend films cast onto PEDOT:PSS-coated ITO slides and excited through the semitransparent ITO electrode. The shoulder in the absorption data around 605 nm is due to interchain excitons on P3HT; the intensity of this peak correlates with the degree of polymer crystallinity. The higher intensity of this shoulder in blends with the **4-Me** (blue circles) and **4-Et** (yellow squares) derivatives is thus in good agreement with the XRD data in Figure 3. As expected, the PL intensity of P3HT (normalized to optical density at 530 nm, green diamonds) is strongly quenched in the BHJ films due to charge transfer at the polymer/fullerene heterointerface. The total amount of exciton quenching is proportional to the effective D/A interfacial area, so that the data show that the **4-Me** and **4-Et** derivatives phase-segregate from P3HT more than **4-iPr** (red point-up triangles) or **4-tBu** (black point-down triangles). The ratios of the integrated PL intensities, however, cannot fully explain the current density differences that we observe under illumination (see text for details).

PAF regions range in size from 50 nm to over 300 nm, and they have heights that are 10−15 nm above the average polymer surface of the film. In contrast, we do not see such features in the BHJs formed from **4-iPr** and **4-tBu**. Instead, we see roughly circular dark regions with an average diameter of ∼14 nm that are interspersed between the P3HT nanocrystallites. Because of the lack of X-ray diffraction from the PAF component of these films, we attribute these features to amorphous PAF-rich regions of the BHJ. Thus, we conclude that the morphology of the BHJs with **4-Me** and **4-Et** is characterized by a large degree of phase segregation, whereas BHJs formed with **4-iPr** and **4-tBu** have significantly more mixing between the P3HT and the fullerene. The question that we will address below is, why do we see such different behavior for **4-Et** and **4-iPr** given that these two molecules differ by only five carbon atoms out of a total of 100−105 carbon atoms per molecule?

Steady-State Photophysics. Figure 5 shows the steady-state photophysics of our P3HT:PAF blend films. The absorption spectra, plotted on the left, are dominated by a large peak between 450 and 650 nm due primarily to P3HT absorption. The shoulder on the red edge near 605 nm has been assigned to the formation of interchain (2D) P3HT excitons, so that the magnitude of this peak correlates with the degree of order of the polymer.[32] The fact that the feature at 605 nm is more pronounced for the P3HT films blended with **4-Et** and **4-Me** is consistent with our assignment of increased phase separation and thus increased polymer crystallinity in these films, as discussed above.

The right side of Figure 5 shows the photoluminescence (PL) spectra of our P3HT:PAF blend films; the PL spectrum of a pure P3HT film is also shown for reference (green diamonds). As expected, the polymer PL is strongly quenched in the presence of the PAFs. The data show that the most crystalline PAFs, **4-Et** and **4-Me**, quench the polymer PL to the lowest degree. This result is consistent with the idea that **4-Me** and **4-Et** are phase segregated on a length scale that is greater than the typical exciton diffusion lengths expected for P3HT in blends with fullerenes derivatives.[33,34] In contrast, the extent of exciton quenching in BHJs prepared from **4-iPr** and **4-tBu** is greater than 90%. This fits with the structural characterization presented above: because **4-iPr** and **4-tBu** do not aggregate into large-scale structures, they remain much more finely dispersed in the polymer phase, providing an increased donor−acceptor interfacial area for splitting P3HT excitons.

It is tempting to correlate differences in J_{sc} observed in devices fabricated from our P3HT:PAF blends (Figure 2) with the degree of exciton quenching seen in Figure 5. Although the general trends correlate well—the short-circuit current is lower for devices based on films that showed the least amount of PL quenching—closer inspection reveals that the ratios of the integrated PL intensities are not sufficiently large to fully explain

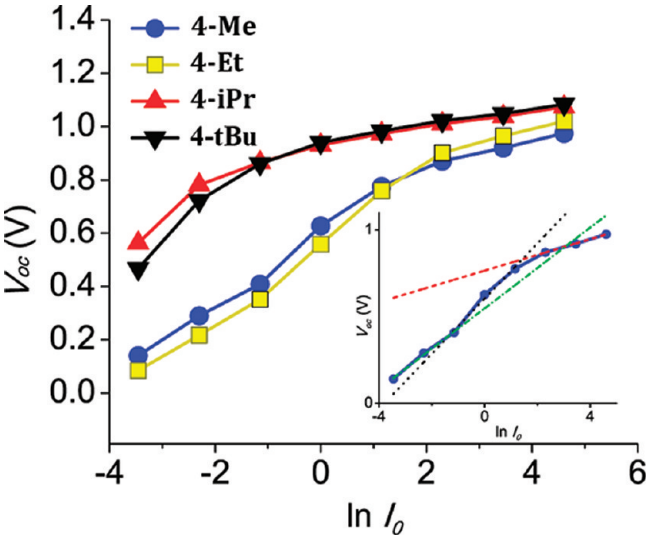

Figure 6. The open-circuit voltage as a function of the natural logarithm of AM 1.5 light intensity. The highest intensity corresponds to 100 mW/cm^2. As with the $J-V$ characteristics, the curves clearly separate into two groups, indicating that different charge recombination mechanisms dominate in the different devices. The data show that solar cells made with **4-Me** and **4-Et** derivatives have a high density of both deep and shallow charge traps and that the trap density is much lower when the **4-tBu** and **4-iPr** derivatives are employed (see text for details). **Inset**: Example of linear fits in the different intensity regions used to probe the recombination mechanism.

the differences in short-circuit currents that we observe. Table 1 shows that the ratio of the J_{sc} values for devices based on **4-tBu** and **4-Et** is fully twice as large as the corresponding PL quenching ratios. We associate the additional drop in J_{sc} for **4-Et** with differences in the effective conductivity of the PAF. This idea fits with the structural characterization of the BHJ films presented above: the large degree of phase segregation observed with **4-Et** and **4-Me** not only leads to reduced exciton harvesting, but it also produces a less interconnected network, leading to reduced carrier extraction from the devices.

Charge Carrier Recombination. If the PAF network morphology is indeed the culprit in explaining the reduced conductivity observed in the devices based on **4-Et** and **4-Me**, then it is reasonable to expect that the poor morphology also would translate into differences in charge carrier recombination. Several groups have used a variety of models to show that the way in which the V_{oc} depends on the incident light intensity, I_0, provides direct information about the recombination kinetics.[35,36] In several models, if the slope of the dependence of V_{oc} on ln I_0 is unity (in units of k_BT/e), then the recombination is largely bimolecular in nature (i.e., dominated by charge carriers that encounter each other long after the initial exciton dissociation event).[36] In contrast, slopes of V_{oc} versus ln I_0 of 2 or greater imply monomolecular recombination (i.e., kinetics dominated by carriers that recombine either geminately or with oppositely charged carriers that are stuck in traps).

Figure 6 shows measurements of V_{oc} vs ln I_0 for our P3HT:PAF BHJ devices, measured over multiple orders of magnitude of the incident AM1.5 light intensity. As with the current−voltage behavior shown in Figure 2, the intensity-dependent V_{oc} behavior of our devices falls into two distinct groups, with the BHJs made with **4-tBu** or **4-iPr** showing distinctly different behavior than the devices made with **4-Et** or **4-Me**. We have fit the linear regions on these plots, as shown in Figure 6 (inset). At the highest intensities (close to 1 sun = 100 mW/cm^2), the slope of V_{oc} with ln I_0 for the devices fabricated with **4-iPr** or **4-tBu** is ~1.2 k_BT/e, which is close to what is expected if bimolecular recombination is the dominant mechanism of charge carrier loss in BHJ solar cells. We note that we, and others,[37] have measured similar slopes of near unity for annealed P3HT:[60]PCBM BHJ solar cells. This slope persists down to intensities that are 5 orders of magnitude less than the standard 100 mW/cm^2 illumination conditions, until at quite low intensities the slope increases dramatically, yielding values of 7.3 and 8.6 k_BT/e for **4-iPr** and **4-tBu**, respectively. This increase in slope indicates that some trap states must be present in the interpenetrating polymer/PAF network morphology in these devices. The fact that the slope increase happens only at very low light intensities, however, indicates that the concentration of the traps is relatively low, since they can be saturated with only a modest number of charge carriers.

In contrast to the behavior observed in BHJ solar cells based on **4-tBu** or **4-iPr**, Figure 6 also shows the behavior of V_{oc} with incident light intensity for devices based on **4-Me** or **4-Et**. These data exhibit an unusual S-shape. This type of behavior has been observed previously in dye-sensitized photovoltaic devices.[38] In particular, the authors in ref 35 developed a model that recreates the S-shape by invoking the existence of deep traps, which can be filled at low light intensities, and a distribution of shallow traps, whose population at intermediate light intensities gives rise to a continuously changing slope of V_{oc} with ln I_0. In this model, the final slope decrease results from the presumed onset of bimolecular recombination at the highest light intensities.

On the basis of these ideas, we propose the following connection between BHJ blend morphology and charge carrier recombination. In films fabricated from **4-Et** or **4-Me**, the large-scale crystallization of the PAF and concomitant phase segregation results in the formation of large isolated PAF islands and/or dead ends in the fullerene network.[39] Large crystalline grains and/or dead ends presumably act as deep electron traps, accounting for the monomolecular recombination behavior at low light intensities. At intermediate light intensities, the deep traps fill, and the grain boundaries between connected PAF crystallites lead to a multitude of shallow traps whose energies are a function of the specific arrangement of local PAF contacts, explaining the variable slope of the V_{oc} versus ln I_0 behavior of these devices. Finally, at high intensities approaching standard illumination conditions, bimolecular recombination becomes a significant loss mechanism, which results in the decreased slope of V_{oc} versus the natural log of incident light intensity. In contrast, the devices made with **4-iPr** or **4-tBu** show largely linear V_{oc} versus ln I_0 behavior due to the absence of large PAF crystallites and the formation of a more interconnected fullerene network, which greatly reduces the density of deep trap states. With more homogeneous mixing of the P3HT and PAF components in these devices, there is also a decrease of the degree of disorder in the shallow traps relative to the cases with **4-Et** or **4-Me**. All of this is consistent with the fact that the photocurrents generated in the **4-Et**- or **4-Me**-based devices are lower than what would be simply predicted on the basis of exciton quenching relative to the devices based on **4-tBu** or **4-iPr**. The different BHJ morphologies with different PAFs lead to different conduction and recombination mechanisms as well as different degrees of exciton harvesting, explaining the large difference in device performance that

results from relatively small changes in the molecular structure of the fullerene.

DISCUSSION

All of the above data make it clear that successive additions of large alkyl groups to the peripheral feathers of the PAFs can cause large changes in the nanoscale morphology of the resultant BHJ film, leading to correspondingly large changes in the performance of polymer/PAF photovoltaic devices. This brings up two important questions. First, what are the physical interactions by which a small increase in the size of the alkyl groups can alter the nanostructure of a BHJ composite to such a great extent? Second, how should one design a fullerene derivative to best utilize these interactions to optimize BHJ morphology for maximum photovoltaic performance? We believe that the relevant physical interactions result from a complex interplay of several factors, including the propensity of the fullerene derivative to either crystallize or self-assemble, and the miscibility of the fullerene derivative with conjugated polymers like P3HT. In this section, we consider how each of these factors can contribute to the structure and function of BHJ solar cells produced with P3HT and different fullerene derivatives.

To optimize fullerene derivatives for use in BHJ solar cells, one recently proposed design rule has been to maximize the solution-phase solubility of the fullerene derivative.[15] The ideas behind this proposal are, first, that high solubility is necessary to allow enough fullerene derivative to be present within the composite to form a good interpenetrating network and, second, that better mixing of the fullerene derivative and polymer components in the casting solution will in turn lead to better mixing of the components in the resultant film. Because the four PAFs we have explored in this work have essentially identical frontier molecular orbitals, we can use the device data presented in Figure 2 as a direct test of this solution-solubility design rule. The solubilities of each of the PAFs in *o*-dichlorobenzene (ODCB), the solvent from which our BHJ films were cast, are 7.4, 47.7, 22.2, and 3.8 mg/mL for **4-tBu**, **4iPr**, **4-Et** and **4-Me**, respectively. On the basis of the proposed solubility design rule, we would expect the morphology of the BHJs based on the most soluble derivatives to show the least degree of phase segregation. Instead, we find that the two most soluble PAFs are **4-iPr** and **4-Et**, yet these two molecules produce very different degrees of phase separation in the BHJ films. Moreover, we also see that the best-mixed (i.e., least phase segregated) BHJ films are produced with **4-tBu**, which is one of the least soluble of the PAF series. Clearly, solution-phase solubility is not the primary factor determining the nanometer-scale morphology of polymer/fullerene derivative BHJ composites.

One of the reasons we chose PAFs for this study is that some members of this class of molecules have a high propensity to self-assemble into one-dimensional stacks, with the ball of one fullerene nestled in the cup formed by the five pendant aryl groups of the adjacent molecule.[23,40,41] In a previous report, we showed that the use of such stacking interactions could lead to improved solar cell performance.[22] We also found that the propensity for PAFs to stack could be tuned by controlling the shape of the "cup" by varying the nature of the aryl group.[22] Quantifying the degree to which different PAFs prefer to stack is a rather challenging endeavor, but we can get some sense for the propensity for self-assembly by examining different crystal structures for the same PAF molecule obtained on single crystals grown from different solvents.[23] We have found that although all four of our PAFs can form one-dimensional columnar stacks in the solid state when crystallized from a particular solvent system, only **4-tBu** stacks consistently in the solid state no matter the solvent system. The propensity for **4-tBu** to crystallize with a columnar stacking motif may also explain why it is relatively insoluble in ODCB, despite the fact that it has the largest alkyl substituent: aggregates of **4-tBu** (i.e., partial stacks) should be much less soluble in typical organic solvents than isolated **4-tBu** molecules.

Although **4-iPr** does not show a columnar stacking motif in every crystal structure obtained, it also has been observed to form stacks from more than one solvent or solvent combination.[23] By contrast, both **4-Me** and **4-Et** show a much broader diversity of crystal structures, including dimers, sheets, and zigzag stacks. On the basis of these crystal structures, the device performance, and the structural data presented in Figures 2−6 above, we hypothesize that under the nonequilibrium conditions of BHJ formation, both **4-iPr** and **4-tBu** self-assemble into an aggregated morphology (likely stacks or bundles of stacks) while **4-Me** and **4-Et** remain more weakly interacting.

How can the propensity of the PAFs to self-assemble affect the morphology of BHJ blends of these molecules with conjugated polymers? It seems likely that any self-assembled PAF subunits that form in solution are likely to survive the spin-casting process and persist into the BHJ film. Self-assembly or stack formation also can take place during solvent evaporation or during thermal annealing. Indeed, PAFs appear to have rather high diffusion constants within the P3HT network, as evidenced by the fact that annealing is essentially complete after just 5 min.[22] Due to their size, however, the self-assembled PAF stacks should be much less mobile in the polymer phase during solvent evaporation or thermal annealing than single PAF molecules. Thus, self-assembled PAFs should be much less likely to form large-scale crystallites, remaining more dispersed through the BHJ, presumably resulting in the formation of a better interpenetrating network. Moreover, the presence of assembled PAF species also likely inhibits the physical mobility of polymer chains during annealing, decreasing polymer crystallinity and thus producing an overall blend structure that is not overly phase-segregated on the nanometer length scale. Conversely, for nonassembling fullerene derivatives, the polymer crystallization that occurs during thermal annealing should produce significant fullerene aggregation. The high physical diffusion of single fullerene molecules through the polymer also likely increases the tendency for aggregated fullerene derivatives to crystallize. Thus, the mutual crystallization of nonassembling fullerene derivatives and conjugated polymers produces an overall BHJ morphology that is highly phase-segregated; if the phase segregation is too extreme, the result is a very poor interpenetrating network.

In addition to self-assembly, the physical miscibility of different fullerene derivatives with conjugated polymers also could have an effect on the nanoscale morphology of BHJ blend films. For example, Moulé and Meerholtz have discussed how controlling phase separation in BHJ blends by preassembling the polymer controls both local morphology and device performance.[42] We would expect that the larger the alkyl substituent, the more miscible the PAF should be with the hexyl side chains of P3HT, so that **4-tBu** and **4-iPr** should be more miscible with the polymer than **4-Et** and **4-Me**. This suggests that there should be a monotonic increase in mixing with the effective van der Waals surface area of the alkyl groups. However, the distinctive

grouping of the PAFs into two classes—good network formers and poor network formers—suggests that PAF solubility alone is insufficient to explain the trends in the data.

Finally, it is worth noting that although we can clearly state that BHJs produced from **4-Et** and **4-Me** are overly phase segregated and that BHJs produced from **4-tBu** and **4-iPr** are much less phase separated, we do not know if the **4-tBu** and **4-iPr** networks are ideal. Indeed, the best performance achieved with these PAF based BHJs is significantly lower than the best performance achievable in [60]PCBM:P3HT BHJ devices.[21] This suggests that the PAF-based BHJs have either over phase separated or overly blended networks. We note, however, that the degree of P3HT crystallinity in annealed **4-tBu** and **4-iPr** based BHJs is very similar to that observed in [60]PCBM:P3HT BHJs.[43] As a result, we believe that it is more likely that the reduced device performance is due to lower intrinsic carrier mobilities in PAFs relative to materials such as [60]PCBM. Reduced electron mobility in the PAFs might result from the fact that the five aryl groups of the PAFs reduce the overlap between the LUMOs of adjacent molecules (even when the molecules are self-assembled), as verified by quantum chemistry calculations.[44] PAFs are thus unlikely to replace PCBM or other high-performance electron acceptors in semiconducting polymer-based photovoltaics. Instead, they provide a good system for studying the effects of fullerene aggregation and assembly on network formation in polymer:fullerene blends. The fact that assembly appears to suppress phase separation even with highly diffusive fullerenes suggests that the use of self-assembly is a viable route to the production of robust BHJ networks.

CONCLUSIONS

In this paper, we have presented an investigation of the structural and optoelectronic properties of a series of polymer/PAF BHJ solar cells that use P3HT as the donor and a novel series of four pentaarylfullerene derivatives as the acceptor. Since the frontier molecular orbitals of the four PAFs are essentially identical, we have had the opportunity to examine how the physical structure of different PAFs produces specific BHJ morphologies and how these morphologies ultimately affect device performance. We found that the four PAFs examined produced BHJ blends with two distinct morphologies. Structural studies (X-ray diffraction and AFM) showed that **4-Et** and **4-Me** have highly phase-segregated nonideal nanoscale morphologies. In contrast, **4-tBu** and **4-iPr** remain interspersed with the polymer.

The different BHJ morphologies formed by the different PAFs are directly responsible for dramatic differences in photovoltaic performance. The large amount of phase segregation seen with **4-Et** and **4-Me** leads to a low degree of PL quenching and thus poor exciton harvesting, which in turn produced low short-circuit currents. We also find that the overly phase segregated morphology produced with the **4-Et** or **4-Me** blends is associated with a high carrier trap density, which leads to an even further decrease in the photocurrent. In contrast, the better mixing of the polymer with **4-tBu** and **4-iPr** leads to better exciton harvesting, as well as the formation of a better interpenetrating network with a lower carrier trap density.

We also have found that simple concepts, such as the solubility of the fullerene, are not terribly useful in predicting the type of network formed in BHJ blends. Instead, we consider the propensity of the various PAFs to self-assemble into columnar stacks as having a much more direct degree of control over the nanometer-scale morphology of a BHJ blend: we hypothesize that self-organization of molecules like **4-tBu** and **4-iPr** to form aggregates that have low diffusivity in the P3HT network provides a viable route to preventing overphase separation in semiconducting polymer-based BHJ networks. Thus, even though it is possible to anneal [60]PCBM to form a nearly ideal network with P3HT through random phase separation, the annealing step is not kinetically robust so that the best device performance cannot be easily reproduced in other laboratories or in a large scale factory setting.[45] The work presented here provides an alternative route to network formation. So, even though PAFs do not produce the highest efficiency solar cells, we believe that future molecules that build on these self-assembly ideas will be able to produce higher efficiency devices with more robust BHJ networks. Such robust networks should be more easily scaled to industrial production without reduction in performance relative to systems that rely on spontaneous phase donor/acceptor segregation.

ACKNOWLEDGMENT

This work was supported by the Department of Energy through an Energy Frontiers Research Center (EFRC) under Contract No. DE-SC0001342:001. Partial support for some coauthors on this paper also was received from the National Science Foundation under Grant Number CHE-0527015. Portions of this research were carried out at the Stanford Synchrotron Radiation Laboratory, a national user facility operated by Stanford University on behalf of the U.S. Department of Energy, Office of Basic Energy Sciences.

REFERENCES

(1) Dennler, G; Scharber, M.; Brabec, C. J. *Adv. Mater.* **2009**, *21*, 1323.
(2) Yao, Y.; Hou, J.; Xu, Z.; Li, G.; Yang, Y. *Adv. Funct. Mater.* **2008**, *18*, 1783.
(3) Hwang, I; Cho, S.; Kim, J.; Lee, K.; Coates, N.; Moses, D.; Heeger, A. J. *J. Appl. Phys.* **2008**, *104*, 033706.
(4) Günes, S.; Nuegebauer, H.; Sarichiftichi, N. S. *Chem. Rev.* **2007**, *107*, 1324.
(5) Yang, C. Y.; Heeger, A. J. *J. Synth. Met.* **1996**, *83*, 85.
(6) Shaw, P. E.; Ruseckas, A.; Samuel, I. D. W. *Adv. Mater.* **2008**, *20*, 3516.
(7) Huijser, A.; Savenije, T. J.; Shalav, A.; Siebelles, L. D. *J. Appl. Phys.* **2008**, *104*, 034505.
(8) Yu, G.; Gao, J.; Hummelen, J. C.; Wudl, F.; Heeger, A. J. *Science* **1995**, *270*, 1789.
(9) Ayzner, A. L.; Tassone, C. J.; Tolbert, S. H.; Schwartz, B. J. *J. Phys. Chem.* **2009**, *113*, 20050.
(10) Lee, K. H.; Schwenn, P. E.; Smith, A. R. G.; Cavaye, H.; Shaw, P. E.; James, M.; Krueger, K. B.; Gentle, I. R.; Meredith, P.; Burn, P. L. *Adv. Mater.* **2011**, *23*, 766.
(11) Verploegen, E.; Mondal, R.; Bettinger, C. J.; Sok, S.; Toney, M. F.; Bao, Z. *Adv. Funct. Mater.* **2010**, *20*, 3519.
(12) Ma, W. L.; Yang, C. Y.; Gong, X.; Lee, K.; Heeger, A. J. *Adv. Funct. Mater.* **2005**, *15*, 1617.
(13) Peet, J.; Kim, J. Y.; Coates, N. E.; Ma, W. L.; Moses, D.; Heeger, A. J.; Bazan, G. C. *Nat. Mater.* **2007**, *6*, 497.
(14) Salim, T.; Wong, L. H.; Bräuer, B.; Kukreja, R.; Foo, Y. L.; Bao, Z.; Lam, Y. M. *J. Mater. Chem.* **2011**, *21*, 242.
(15) Liang, Y; Feng, D.; Guo, J.; Szarko, J. M.; Ray, C.; Chen, L. X.; Yu, L. *J. Am. Chem.* **2009**, *131*, 56.

(16) Troshin, P. A.; Hoppe, H.; Renz, J.; Egginger, M.; Mayorova, J. Y.; Goryachev, A. E.; Peregudov, A. S.; Lyubovskaya, R. N.; Gobsch, G.; Sariciftci, N. S.; Razumov, V. F. *Adv. Funct. Mater.* **2009**, *19*, 779.
(17) Zhang, Y.; Yip, H. L.; Acton, O.; Hau, S. K.; Huang, F.; Jen *Chem. Mater.* **2009**, *21*, 2598.
(18) Kooistra, F. B.; KNol, J.; Kastenberg, F.; Popescu, L. M.; Verhees, W. J. H.; Kroon, J. M.; Hummelen, J. C. *Org. Lett.* **2007**, *9*, 551.
(19) Li, G.; Shrotiya, V.; Yao, Y.; Huang, J.; Yang, Y. *J. Mater. Chem.* **2007**, *17*, 3126.
(20) Swinnen, A.; Haeldermans, I.; Vanlaeke, P.; D'Haen, J. D.; Poortmans, J.; D'Olieslaegger, M.; Manca, J. V. *Eur. Phys. J. Appl. Phys.* **2007**, *36*, 251.
(21) Wienk, M. M.; Kroon, J. M.; Verhees, W. J. H.; Knol, J.; Hummelen, J. C.; Van Hal, A.; Janssen, R. A. J. *Angew. Chem., Int. Ed.* **2003**, *42*, 3371.
(22) Kennedy, R. D.; Ayzner, A. L.; Wanger, D. D.; Day, C. T.; Halim, M.; Khan, S. I.; Tolbert, S. H.; Schwartz, B. J.; Rubin, Y. *J. Am. Chem. Soc.* **2008**, *130*, 17290.
(23) Kennedy, R. D.; Halim, M.; Khan, S. I.; Schwartz, B. J.; Tolbert, S. H.; Rubin, Y. *Chem. Eur. J.* **2011**, submitted.
(24) Sawamura, M.; Kawai, K.; Matsuo, Y.; Kanie, K.; Kato, T.; Nakamura, E. *Nature* **2002**, *419*, 702.
(25) Matsuo, Y.; Sato, Y.; Hasiguchi, M.; Matsuo, K.; Nakamura, E. *Adv. Funct. Mater.* **2009**, *19*, 2224.
(26) Woo, C. H.; Thompson, B. C.; Kim, B. J.; Toney, M. F.; Freschet, M. J. *J. Am. Chem. Soc.* **2008**, *130*, 16324.
(27) Chu, C. W.; Yang, H.; hou, W. J.; Huang, J.; Li, G.; Yang, Y. *Appl. Phys. Lett.* **2008**, *92*, 103306.
(28) Cullity, B. D. *Elements of X-ray Diffraction*; Addison-Wessley: Reading, MA, 1956.
(29) Jo, J.; Kim, S. S.; Na, S. I.; Yu, B. K.; Kim, D. K. *Adv. Funct. Mater.* **2009**, *19*, 866.
(30) Yang, X.; Loos, J.; Veenstra, S. C.; Verhees, W. J. H.; Weink, M. M.; Kroon, J. M.; Mechels, M. A. J.; Janssen, R. A. J. *Nano Lett.* **2005**, *5*, 579.
(31) Yang, H.; Shin, T. J.; Bao, Z.; Ryu, C. *J. Polym. Sci., Part B: Polym. Phys.* **2007**, *45*, 1303.
(32) Brown, P. J.; Thomas, D. S.; Köhler, A.; Wilson, J. S.; Kim, J.-S.; Ramsdale, C. M.; Sirringhaus, H.; Friend, R. H. *Phys. Rev. B* **2000**, *67*, 064203.
(33) Shaw, P. E.; Ruseckas, A.; Samuel, I. D. W. *Adv. Mater.* **2008**, *20*, 3516.
(34) Ruseckas, A.; Shaw, P. E.; Samuel, I. D. W. *Dalton Trans.* **2009**, 10040.
(35) Cheyns, D.; Poortmans, J.; Heremans, P.; Deibel, C.; Verlaak, S.; Rand, B. P.; Genoe, J. *Phys. Rev. B* **2008**, *77*, 165332.
(36) Mandoc, M. M.; Veurman, W.; Koster, L. J. A.; de Boer, B.; Blom, P. W. M. *Adv. Funct. Mater.* **2007**, *17*, 2167.
(37) Koster, L. J. A.; Mihailetchi, V. D.; Ramaker, R.; Blom, P. W. M. *Appl. Phys. Lett.* **2005**, *86*, 123509.
(38) Salvador, P.; Hidalgo, M. G.; Zaban, A.; Bisquert, J. *J. Phys. Chem. B* **2005**, *109*, 15915.
(39) Ayzner, A. L.; Wanger, D. D.; Tassone, C. J.; Tolbert, S. H.; Schwartz, B. J. *J. Phys. Chem. C* **2008**, *112*, 18711.
(40) Peroukidis, S. D.; Vanakaras, A. G.; Photinos, D. J. *J. Chem. Phys.* **2005**, *123*, 164904.
(41) Matsuo, Y.; Muramatsu, A.; Hamasaki, R.; Mizoshita, N.; Kato, T.; Nakamura, E. *J. Am. Chem. Soc.* **2004**, *126*, 432.
(42) Moulé, A. J.; Meerholtz, K. *Adv. Funct. Mater.* **2009**, *19*, 1.
(43) Dante, M.; Peet, J.; Nguyen, T. Q. *J. Phys. Chem. C* **2008**, *112*, 7241.
(44) Okada, S.; Arita, R.; Matsuo, Y.; Nakamura, E.; Oshiyama, A.; Aoki, H. *Chem. Phys. Lett.* **2004**, *399*, 157.
(45) Krebs, F. C.; Gevorgyan, S. A.; Alstrup, J. *J. Mater. Chem.* **2009**, *19*, 5442.